

Micro-Macroscopic Coupled Modeling of Batteries and Fuel Cells

II. Application to Nickel-Cadmium and Nickel-Metal Hydride Cells

W. B. Gu and C. Y. Wang*

Department of Mechanical Engineering and Pennsylvania Transportation Institute, The Pennsylvania State University, University Park, Pennsylvania 16802, USA

B. Y. Liaw*

Hawaii Natural Energy Institute, University of Hawaii at Manoa, Honolulu, Hawaii 96822, USA

ABSTRACT

The micro-macroscopic coupled model developed in a companion paper is applied to predict the discharge and charge behaviors of nickel-cadmium (Ni-Cd) and nickel-metal hydride (Ni-MH) cells. The model integrates important microscopic phenomena such as proton or hydrogen diffusion and conduction of electrons in active materials into the macroscopic calculations of species and charge transfer. Simulation results for a full Ni-Cd cell and single MH electrode are presented and validated against the pseudo two-dimensional numerical model in the literature. In good agreement with the previous results, the present family of models is computationally more efficient and is particularly suitable for simulations of complex test conditions, such as the dynamic stress test and pulse charging for electric vehicles. In addition, a mathematical model for full Ni-MH cells is presented and sample simulations are performed for discharge and recharge with oxygen generation and recombination taken into account. These gas reactions represent an important mechanism for battery overcharge in the electric vehicle application.

Introduction

In a companion paper,¹ a micro-macroscopic coupled model to simulate batteries and fuel cells was described. The model is capable of incorporating interfacial nonequilibrium effects present in advanced battery systems and also is a single-domain formulation as all the governing equations are valid in both electrode and separator regions. The latter feature can greatly facilitate numerical implementation and simulation of complete cells, including the negative electrode, separator, and positive electrode, thereby providing an efficient simulation tool. The objective of this paper is to demonstrate various unique features and capabilities of the new model through application to two important battery systems: nickel-cadmium and nickel-metal hydride.

The nickel-cadmium (Ni-Cd) cell is considered to be one of the near-term power sources for electric vehicles, whereas the nickel-metal hydride (Ni-MH) battery is expected to replace the Ni-Cd battery as a promising electric vehicle battery due to its higher energy density, higher power density, longer cycle life, and absence of poisonous heavy metals.² Substantial efforts are currently focused on the development of Ni-MH batteries and the improvement of Ni-Cd batteries. A powerful mathematical model can help to understand the complicated discharge and charge behaviors of these intercalative batteries and thus plays an important role in battery design, scale-up, and optimization.

Several mathematical models have been developed to predict the performance of a single nickel electrode^{3,4} as well as a full Ni-Cd cell.⁵⁻⁸ Extensive reviews were provided therein and thus are not repeated here. Most important, it was found that the proton diffusion and ohmic drop occurring across the active material layer on a microscale control the cell performance and active material utilization, whereas the species transport in the electrolyte on the cell scale was found to have little effect on battery behavior. To take these microscopic phenomena into account, a modified pseudo two-dimensional model based on the macrohomogeneous model of Newman⁹ was proposed by De Vids and White.⁷ In this model, one dimension was defined across the cell (i.e., the "macroscopic" dimension), whereas the other dimension was defined across the active material layer (i.e., the "microscopic" dimension). Fick's law of diffusion and Ohm's law of electronic conduction

were applied along the microscopic coordinate to account for proton diffusion and ohmic drop. A variable electronic conductivity of the nickel electrode was considered because nickel hydroxide is an electrical insulator in its reduced state and a conductor in its oxidized state. The microscopic equations were then coupled to the macroscopic governing equations for species and charge transfer across the cell, and together they were numerically solved simultaneously. While such a pseudo two-dimensional approach is capable of incorporating microscopic phenomena into a macroscopic model, it is computationally demanding and appears difficult to apply to practical situations wherein complex discharge or charge modes are involved as in electric vehicle applications.

Efforts were made to find a more computationally efficient way of accounting for proton diffusion and conduction of electrons on the scale of active material particles.^{4,8} In these efforts, the microscopic diffusion equation was solved by Laplace transforms based on the simplified planar treatment for the solid phase, and an integral expression of the potential was obtained from the conservation equation of charge inside the nickel active material.⁴ Both local solutions are in semianalytical forms and require numerical evaluation of integrals. These solutions were later integrated into a macrohomogeneous model for species and charge transfer across the cell to simulate the behavior of a full Ni-Cd battery.⁸ It was reported that a stability problem may arise from such a hybridization of numerical integration and differentiation due to the synchronization of the time step required for the microscopic solutions with that used in the numerical simulation of macroscopic species-conservation and charge-conservation equations.

While there has been extensive research on the modeling of Ni-Cd cells, a complete mathematical model for discharge and recharge of Ni-MH cells is still absent.² Limited modeling attempts have been made to simulate the discharge process of a single metal hydride electrode¹⁰⁻¹³ and a Ni-MH cell.¹⁴ Similar to the nickel electrode, hydrogen diffusion in the metal hydride particles is typically a rate-limiting mechanism. Viitanen¹⁰ first developed a mathematical model to describe the polarization behavior of the metal hydride (MH) electrode in the absence of macroscopic ohmic losses and species concentration gradients and numerically simulate the electrode behavior under various conditions. Following their work on the nickel

* Electrochemical Society Active Member.

electrode, Jain and Weidner¹¹ used Laplace transforms to obtain an infinite-series solution for the hydrogen concentration at the particle surface in a MH electrode and simulated the discharge process under the assumption that there are neither macroscopic ohmic losses nor concentration nonuniformities. Their results indicated that the mass diffusion coefficient of hydrogen in MH particles and the particle size are critical parameters affecting the discharge characteristics of the MH electrode. Closely patterning Jain and Weidner's work on Ni-Cd cells, De Vidts et al.¹² presented a pseudo two-dimensional numerical model for the discharge of a single MH electrode. In this work, spherical MH particles were assumed and both macroscopic species and charge-transport and microscopic hydrogen diffusion in MH particles were included. It was found that diffusion of atomic hydrogen from the bulk of MH particles to the particle surface becomes more critical as the discharge rate and/or particle size increase.

Most recently, Heikonen et al.¹³ presented a mathematical model for the discharge of a MH electrode composed of irregularly shaped particles. This work is important in that actual microstructures of the MH electrode are always complex and irregular, whereas a sphere has the least surface area for a given volume. An important part of this analysis was defining an equivalent radius of diffusion as the solid volume fraction (ϵ_s) divided by the specific surface area (a_{se}) in the case of nonspherical particles. It is clear from the discussion in Part I¹ that such a selection of the equivalent radius is an accurate representation of the length scale of electrode microstructures and also is based on better measurable geometrical quantities (i.e., ϵ_s and a_{se}).

At the time this article was being submitted for publication, the authors became aware of a recent attempt by Paxton and Newman¹⁴ to model Ni-MH batteries. They argued that proton diffusion in the nickel electrode is not rate-limiting in the parametric range they examined and therefore was not considered in their model.

In this paper, we apply the micro-macroscopic model developed in Part I to Ni-Cd and Ni-MH cells in order to demonstrate capabilities of the present modeling approach, as well as to quantify the utility of the simple constitutive relations developed in Part I. Comparisons to the available data on the discharge of a Ni-Cd cell⁷ and a single MH electrode¹² are made. Finally, a full Ni-MH cell model accounting for both proton diffusion in the nickel electrode and hydrogen diffusion in the MH electrode is presented for the first time, and sample simulations are performed to study the discharge behavior and associated limiting mechanisms, as well as the recharge behavior in the presence of oxygen evolution and recombination. It should be noted that modeling a full Ni-MH cell, with both proton diffusion in the nickel electrode and hydrogen diffusion in the MH electrode taken into account, is computationally a more challenging task than a Ni-Cd cell. The efficiency of the present Ni-Cd and Ni-MH models was further demonstrated in a recent application to simulate a series of complex test regimes, such as the dynamic stress test and federal urban driving schedule designed to evaluate electric vehicle batteries.¹⁵

Micro-Macroscopic Modeling

A Ni-Cd or Ni-MH cell is composed of three regions: a negative electrode, a positive electrode, and a separator in between acting as an electronic insulator, as schematically shown in Fig. 1. Porous nickel oxyhydroxide is used as the active material for the positive electrode in both Ni-Cd and Ni-MH cells, whereas the negative electrode is made of either cadmium powders in the Ni-Cd cell or metal hydride powders in the Ni-MH cell. The electrolyte in both cells commonly is a concentrated KOH aqueous solution. Electrochemical reactions taking place at the electrode/electrolyte interface inside various electrodes during discharge and charge are given as

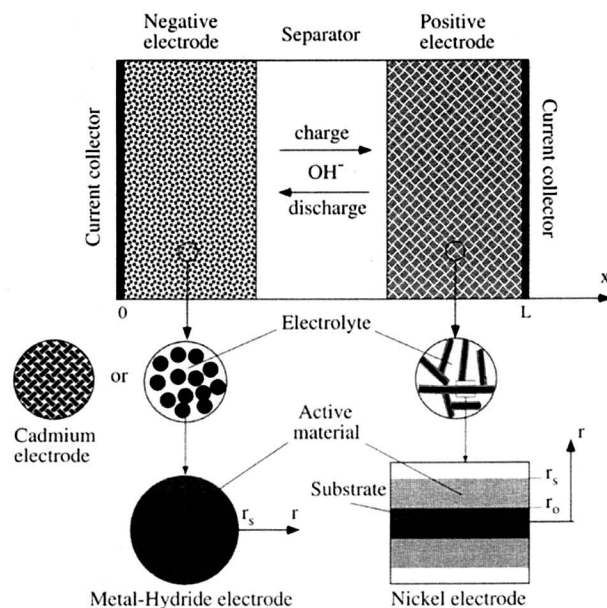
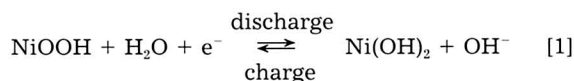
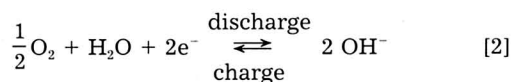


Fig. 1. A schematic diagram of Ni-Cd and Ni-MH cells and the model representation.

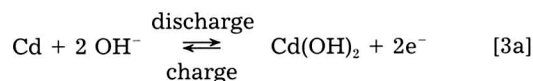
Positive electrode



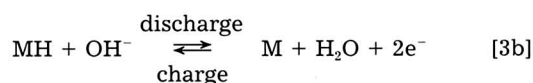
with the side reaction



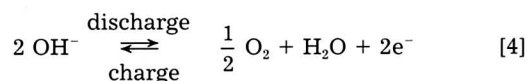
Negative electrode



or



with the same side reaction



Assumptions.—The following assumptions are made for the model development and for the purpose of rigorously comparing with the previous work^{7,12}

1. Each electrode is a two-phase system consisting of the solid matrix and liquid electrolyte, as shown in Fig. 1. Oxygen evolving during electrochemical reactions is dissolved in the liquid phase and treated as a neutral species with an apparent diffusion coefficient.^{5,7,12} This assumption may be unrealistic in some situations but is necessary for comparisons of the present model with previous results.

2. The nickel electrode is modeled to consist of composite cylindrical needles with a substrate inside (see Fig. 1). The porosity variation is neglected.

3. The MH electrode is modeled to consist of spherical particles with uniform size and constant porosity.

4. The convection effect is neglected, leaving the species transport by diffusion and migration only.

5. Interfacial chemical and electrical equilibrium exists in the electrolyte phase due to large values of the mass dif-

fusivity and ionic conductivity in the electrolyte, i.e., $(c_e)^e = \bar{c}_{es}$ and $(\phi_e)^e = \bar{\phi}_{es}$.

6. Thermal effects are discounted.

With these assumptions, one-dimensional forms of the micro-macroscopic model can be extracted from the general framework presented in Part I.¹ In the remainder of this paper, the averaging symbols are dropped for convenience, namely, $(\Phi_k)^k = \Phi_k$, whereas an interfacial quantity is still denoted by an overbar so as to distinguish it from its volume-averaged counterpart. In addition, a superscript is added to c to indicate the concentration of a specific species, e.g., c_s^H , to denote the hydrogen or proton concentration in the solid phase. In the case where a species exists only in one phase, the corresponding subscript is dropped for simplicity, i.e., c^H .

Governing equations.—Reaction rates for the various charge-transfer reactions involved in a Ni-Cd or Ni-MH cell can be derived from the general Butler-Volmer equation with respect to a specified reference state. Following De Vidts and White⁷ and De Vidts et al.,¹² we have

$$\bar{i}_{n1} = i_{ol,ref} \left[\left(\frac{c^{OH}}{c_{ref}^{OH}} \right) \left(\frac{\bar{c}^H}{c_{ref}^H} \right) \exp \left(\frac{\alpha_{a1} F}{RT} \eta_1 \right) - \left(\frac{c_{max}^H}{c_{max}^H - c_{ref}^H} \right) \exp \left(-\frac{\alpha_{c1} F}{RT} \eta_1 \right) \right] \quad [5]$$

$$\bar{i}_{n2} = i_{o2,ref} \left[\left(\frac{c^{OH}}{c_{ref}^{OH}} \right)^2 \exp \left(\frac{\alpha_{a2} F}{RT} \eta_2 \right) - \left(\frac{c^{O_2}}{c_{ref}^{O_2}} \right) \exp \left(-\frac{\alpha_{c2} F}{RT} \eta_2 \right) \right] \quad [6]$$

$$\bar{i}_{n3} = i_{o3,ref} \left[\left(\frac{c^{OH}}{c_{ref}^{OH}} \right)^2 \exp \left(\frac{\alpha_{a3} F}{RT} \eta_3 \right) - \exp \left(-\frac{\alpha_{c3} F}{RT} \eta_3 \right) \right] \quad \text{for Cd electrode} \quad [7a]$$

or

$$\bar{i}_{n3} = i_{o3,ref} \left[\left(\frac{c^{OH}}{c_{ref}^{OH}} \right) \left(\frac{\bar{c}^H}{c_{ref}^H} \right)^{0.67} \exp \left(\frac{\alpha_{a3} F}{RT} \eta_3 \right) - \exp \left(-\frac{\alpha_{c3} F}{RT} \eta_3 \right) \right] \quad \text{for MH electrode} \quad [7b]$$

$$\bar{i}_{n4} = i_{o4,ref} \left[\left(\frac{c^{OH}}{c_{ref}^{OH}} \right)^2 \exp \left(\frac{\alpha_{a4} F}{RT} \eta_4 \right) - \left(\frac{c^{O_2}}{c_{ref}^{O_2}} \right) \exp \left(-\frac{\alpha_{c4} F}{RT} \eta_4 \right) \right] \quad [8]$$

where c 's with various superscripts stand for their concentration and η_j is the surface overpotential of reaction j , i.e.

$$\eta_j = \bar{\phi}_{se} - \phi_e - U_{j,ref} \quad j = 1, 2, 3, \text{ and } 4 \quad [9]$$

Here the interfacial electrical equilibrium condition (i.e., $\bar{\phi}_{es} = \phi_e$) has been used and $U_{j,ref}$ is the open-circuit potential at reference conditions for reaction j .

Species conservation equations.—There are two species that participate in charge-transfer reactions present in the liquid electrolyte under consideration: an ionic species OH^- and a neutral species O_2 . Under the above-mentioned assumptions, the convection term drops off and the interface velocity is equal to zero for a constant porosity. Applying the general volume-averaged conservation equation of species (i.e., Eq. 41 in Part I¹) and making use of the interfacial balance condition (i.e., Eq. 49 in Part I¹) to the two species, respectively, yields

$$\frac{\partial(\epsilon_e c^{OH})}{\partial t} = \nabla \cdot (D_{eff}^{OH} \nabla c^{OH}) + \frac{t^o - 1}{F} j^{OH} \quad [10]$$

$$\frac{\partial(\epsilon_e c^{O_2})}{\partial t} = \nabla \cdot (D_{eff}^{O_2} \nabla c^{O_2}) + \frac{1}{4F} j^{O_2} \quad [11]$$

Here, t^o is the transference number of the OH^- with respect to the velocity of the solvent and D_{eff}^{OH} is an effective diffusion coefficient including the effect of tortuosity, i.e.

$$D_{eff}^{OH} = D^{OH} \epsilon_e^{1.5} \quad [12]$$

where D^{OH} is the mass diffusion coefficient of species OH^- in the electrolyte KOH. Likewise, the effective mass diffusivity of oxygen in Eq. 11 follows the same Bruggeman relation as given in Eq. 12.

The source term in Eq. 10 is proportional to j^{OH} , the total current from all electrochemical reactions that generate or consume the species OH^- at the electrode/electrolyte interface, namely

$$j^{OH} = a_{se} \sum_j \bar{i}_{nj} = \begin{cases} a_{Ni}(\bar{i}_{n1} + \bar{i}_{n2}) & \text{in the nickel electrode} \\ 0 & \text{in the separator} \\ (a_{Cd} \text{ or } a_{MH})(\bar{i}_{n3} + \bar{i}_{n4}) & \text{in the Cd or MH electrode} \end{cases} \quad [13]$$

Similarly, j^{O_2} is the transfer current associated with the generation or consumption of oxygen, i.e.

$$j^{O_2} = \begin{cases} a_{Ni} \bar{i}_{n2} & \text{in the nickel electrode} \\ 0 & \text{in the separator} \\ (a_{Cd} \text{ or } a_{MH}) \bar{i}_{n4} & \text{in the Cd or MH electrode} \end{cases} \quad [14]$$

In addition, one species, either proton or atomic hydrogen, is present in the solid phase of the nickel and MH electrodes, respectively. This species is represented by a uniform symbol, H, in the present work. Similarly to for species OH^- and O_2 , we have

$$\frac{\partial(\epsilon_s c^H)}{\partial t} = \nabla \cdot (D_{eff}^H \nabla c^H) + \frac{j^H}{F} \quad [15]$$

where

$$j^H = \begin{cases} a_{Ni} \bar{i}_{n1} & \text{in the nickel electrode} \\ 0 & \text{in the separator} \\ a_{MH} \bar{i}_{n3} & \text{in the MH electrode} \end{cases} \quad [16]$$

The interfacial balance of H in either nickel or MH electrode becomes

$$\frac{D^H}{l_{se}} (\bar{c}_{se}^H - c^H) = \frac{j^H}{a_{se} F} \quad [17]$$

where \bar{c}_{se}^H is the proton or hydrogen concentration at the electrode/electrolyte interface and l_{se} is the diffusion length, the expressions of which have been derived as follows¹

$$l_{se} = \frac{r_s + r_o}{4} - \frac{r_s r_o}{3(r_s - r_o)} + \frac{2r_o^3}{3(r_s^2 - r_o^2)} \quad [18]$$

for the cylindrical morphology of the nickel electrode and

$$l_{se} = \frac{r_s}{5} \quad [19]$$

for the spherical morphology of the MH electrode.

Although we have formally included species diffusion on a macroscopic scale in Eq. 15 (i.e., the first term on the right side), in practice this term may be negligible because the microscopic species diffusion length is much smaller than the characteristic length for diffusion into or out of an averaging volume. Mathematically, this can be shown by comparing the magnitudes of the macroscopic diffusion term and interfacial transfer term due to diffusion as

expressed by Eq. 17. Noting that the specific interfacial area, a_{se} , and the diffusion length, l_{se} , are proportional to $1/r_s$ and r_s , respectively, where r_s is a representative microscopic length, the ratio of the magnitudes of the two terms is

$$\frac{\nabla \cdot (D_{eff}^H \nabla c^H)}{j^H/F} = \frac{\nabla \cdot (D_{eff}^H \nabla c^H)}{a_{se} D^H (\bar{c}_{se}^H - c^H) l_{se}} \approx \frac{D_{eff}^H \Delta c^H / L_e^2}{D^H \Delta c^H / r_s^2} \approx \frac{r_s^2}{L_e^2} \ll 1 \quad [20]$$

where L_e is a macroscopic length (e.g., the electrode thickness) and Δc^H stands for a suitable concentration scale. Hence, Eq. 15 can be further simplified to

$$\frac{\partial(\epsilon_s c^H)}{\partial t} = \frac{j^H}{F} \quad [21]$$

Charge conservation equations.—Application of the general charge-conservation equation derived in Part I to the solution phase under consideration yields¹

$$\nabla \cdot (\kappa^{eff} \nabla \phi_e) + \nabla \cdot (\kappa_D^{eff} \nabla \ln c^{OH}) + j^{OH} = 0 \quad [22]$$

This equation can be used to determine the electrical potential in the electrolyte phase, ϕ_e . Here, the effective ionic conductivity is given by $\kappa^{eff} = \epsilon_e^{1.5} \kappa$ following Eq. 12, whereas κ_D^{eff} is the diffusional conductivity given by

$$\kappa_D^{eff} = \frac{2RT\kappa^{eff}}{F} \left(1 + \frac{d \ln f_{\pm}}{d \ln c^{OH}} \right) \left(1 - t^{\circ} + \frac{c^{OH}}{2c^{H_2O}} \right) \quad [23]$$

The transfer current in Eq. 22, j^{OH} , is the same as given in Eq. 13.

For the solid phase, the charge-conservation equation can be written as¹

$$\nabla \cdot (\sigma^{eff} \nabla \phi_s) - j^{OH} + a_{sb} \frac{\bar{\phi}_{sb} - \phi_s}{R_{sb}} = 0 \quad [24]$$

where the second term represents the transfer current generated at the electrode/electrolyte interface, and the third term stands for the current conducted into a substrate, with a_{sb} and $\bar{\phi}_{sb}$ being the specific area and potential at the active material/substrate interface. This term is absent on the cadmium and MH electrodes and is relevant only in the nickel electrode where a substrate is embedded in the solid material to improve the electronic conductivity. In this case, the substrate potential $\bar{\phi}_{sb}$ usually remains constant due to a large value of electronic conductivity.

In addition to the two volume-averaged conservation equations for charge, the interfacial charge balance at the electrode/electrolyte interface is also needed and now becomes¹

$$\frac{\bar{\phi}_{se} - \phi_s}{R_{se}} = -\frac{j^{OH}}{a_{se}} \quad [25]$$

where $\bar{\phi}_{se}$ is the solid potential at the interface and is needed to calculate the interfacial overpotential, η . As noted earlier, the electric resistances appearing in Eq. 24 and 25 are directly proportional to the particle size of the active material and inversely proportional to the electronic conductivity¹ (also see the following discussion). For both cadmium and MH electrodes, the respective electronic conductivities are sufficiently high that the electric resistance, R_{se} , approaches zero, and hence Eq. 25 essentially reduces to

$$\bar{\phi}_{se} = \phi_s \quad [26]$$

That is, electrical equilibrium exists in cadmium and MH electrodes. In contrast, the nickel electrode in the semi-conducting state has a relatively low electronic conductivity so that electrical equilibrium does not hold true. In this case, the microscopic electrical resistances derived by Wang et al.¹ can be used

$$R_{sb} = \frac{r_o}{12} \left(\frac{r_s - r_o}{r_s + r_o} \right) \left(\frac{5r_s + 3r_o}{\sigma_o r_o} + \frac{3r_s + r_o}{\sigma_s r_s} \right) \quad [27]$$

and

$$R_{se} = \frac{r_s}{12} \left(\frac{r_s - r_o}{r_s + r_o} \right) \left(\frac{r_s + 3r_o}{\sigma_o r_o} + \frac{3r_s + 5r_o}{\sigma_s r_s} \right) \quad [28]$$

where σ_o and σ_s denote the conductivities of the nickel active materials at the electrode/substrate and electrode/electrolyte interfaces, respectively.

The effective conductivity of the solid phase in Eq. 24, σ^{eff} , is related to the conductivity of the active materials, σ , by^{7,12}

$$\sigma^{eff} = \epsilon_s \sigma \quad s = \text{Ni or MH} \quad [29]$$

where s denotes the nickel and MH electrodes, respectively, and

$$\sigma^{eff} = \sigma \left(\frac{\epsilon_{Cd} - \epsilon_{Cd,min}}{\epsilon_{Cd,max} - \epsilon_{Cd,min}} \right)^{\beta} \quad [30]$$

for cadmium electrode. The conductivity of the nickel active material is a strong function of local state of charge,⁷ i.e.

$$\sigma = 0.1185 \exp \left[-8.459 \left(\frac{c^H}{c_{max}^H} \right)^4 \right] \quad [31]$$

whereas the conductivities of the pure cadmium and MH alloy are assumed to be constant at the values of 1.4706×10^5 S/cm and 41505.1 S/cm, respectively.^{7,12} The effective conductivity of either MH or cadmium electrode is thus sufficiently high, leading to a virtually uniform potential distribution across the electrode.

The term β in Eq. 30 is a tortuosity factor associated with the porous structure of the cadmium electrode. A value of 0.5 for β is taken from Ref. 12. The porosity of the cadmium electrode assumes maximum and minimum values at full charge and discharge, respectively. In between, the porosity is calculated from the porosity variation equation to be shown below to account for structural change.

Porosity variation equation.—Whereas the porosity is assumed constant on the nickel and MH electrodes, the porosity of the cadmium electrode varies as a result of the charge-transfer reaction during cell operation, as described by Eq. 26 in Part I,¹ namely

$$\frac{\partial \epsilon_s}{\partial t} = \frac{1}{2F} \left(\frac{M_r^{Cd}}{\rho^{Cd}} - \frac{M_r^{Cd(OH)_2}}{\rho^{Cd(OH)_2}} \right) a_{Cd} \bar{i}_{n3} \quad [32]$$

with a_{Cd} being the specific interfacial area and varying with the porosity of the electrode

$$a_{Cd} = a_{Cd,max} \left(\frac{\epsilon_{Cd} - \epsilon_{Cd,min}}{\epsilon_{Cd,max} - \epsilon_{Cd,min}} \right)^{\tau} \quad [33]$$

where $a_{Cd,max}$ is the specific interfacial area in the cadmium electrode at full charge and τ is an exponent to account for surface passivation and is equal to unity in this study.

In summary, a total of five governing equations, Eq. 10, 11, 15, or 21, 22–24, are developed to solve for the five unknowns: c^{OH} , c^{O_2} , c^H , ϕ_e , and ϕ_s . In addition, two interfacial balances, Eq. 17 and 25, are provided to determine two interfacial quantities: \bar{c}_{se}^H and $\bar{\phi}_{se}$.

Initial/boundary conditions.—Uniform initial conditions are assumed as

$$c^{OH} = c_o^{OH}, c^{O_2} = c_o^{O_2}, c^H = c_o^H \quad [34]$$

Boundary conditions at the positive electrode/current collector boundary ($x = L$) include

$$\frac{\partial c^{\text{OH}}}{\partial x} = 0, \frac{\partial c^{\text{O}_2}}{\partial x} = 0, \frac{\partial c^{\text{H}}}{\partial x} = 0, \frac{\partial \phi_e}{\partial x} = 0, \text{ and } \phi_s = \bar{\phi}_{\text{sb}} \quad [35]$$

At the negative electrode ($x = 0$), there is no flux of species and all current goes through the solid phase

$$\frac{\partial c^{\text{OH}}}{\partial x} = 0, \frac{\partial c^{\text{O}_2}}{\partial x} = 0, \frac{\partial c^{\text{H}}}{\partial x} = 0, \frac{\partial \phi_e}{\partial x} = 0, \quad \text{and } -\sigma^{\text{eff}} \frac{\partial \phi_s}{\partial x} = I \quad [36]$$

For a single MH electrode problem without oxygen generation and recombination as studied by De Vidts et al.,¹² boundary conditions at the interface between the MH electrode and electrolyte reservoir are needed and given by

$$c^{\text{OH}} = c_o^{\text{OH}}, \frac{\partial c^{\text{H}}}{\partial x} = 0, -\kappa^{\text{eff}} \frac{\partial \phi_e}{\partial x} - \kappa_D^{\text{eff}} \frac{\partial \ln c^{\text{OH}}}{\partial x} = I, \text{ and } \frac{\partial \phi_s}{\partial x} = 0 \text{ at } x = L_e \quad [37]$$

where L_e is the thickness of the MH electrode.

Numerical Procedures

The equations in the micro-macroscopic model presented above were discretized by a finite-volume method¹⁵ and solved using a general-purpose computational fluid dynamics (CFD) code. A key feature of the numerical procedures and the corresponding code is that all governing equations are cast into the following general form

$$\frac{\partial(\epsilon\Phi)}{\partial t} = \nabla \cdot (\Gamma \nabla \Phi) + S \quad [38]$$

where Φ represents a general conservable quantity, Γ is a diffusion coefficient pertinent to Φ , and S is a source term. As an example, compare Eq. 38 with the electrolyte concentration equation, Eq. 10. Apparently, Φ stands for the electrolyte concentration, c^{OH} , $\Gamma = D^{\text{OH}}$ is the effective mass diffusivity, and S denotes the species generation term in Eq. 10. For the two charge-conservation equations, the transient term in Eq. 38 vanishes due to the neglect of double-layer charging.

Often, the general source term S in Eq. 38 is a nonlinear function of the dependent variable Φ itself. For example, in the case of the charge-conservation equations for both solid and solution phases, S represents the transfer current which depends on the electrical potentials ϕ_s and ϕ_e in the form of the Butler-Volmer equation. In such situations, it is desirable to linearize the source term using the Taylor series expansion for the iteration process, i.e.

$$S = S(\Phi^o) + \frac{\partial S}{\partial \Phi}(\Phi - \Phi^o) = S_c + S_p \Phi \quad [39]$$

where Φ^o is the value of Φ in the previous iteration, while the constant part, S_c , and the linear coefficient, S_p , are given by

$$S_c = \left[S(\Phi^o) - \frac{\partial S}{\partial \Phi} \Phi^o \right] \text{ and } S_p = \frac{\partial S}{\partial \Phi} \quad [40]$$

Note that S_p must not be positive in this treatment; otherwise, a convergent solution is impossible.¹⁶

The one-dimensional rectangular physical domain was divided by either uniform or nonuniform grid lines. Stringent numerical tests were performed in each case to ensure that the solutions are independent of the grid size and time step. It was found that the typical number of grid lines across the cell width is about 60 (i.e., the size of a finite volume is about 1/20 of an electrode thickness) and the time step normally ranges from 10 to 20 s, except near the end of discharge when smaller time steps are required. The equations were solved as a simultaneous set, and convergence was considered to be reached when the relative

error in each field between two consecutive iterations was less than 10^{-3} . A typical transient simulation for one-dimensional problems required about 10 s of CPU time on an HP BO 160L workstation (160 MHz CPU, SPECfp95 7.39). Such CPU time is quite manageable and permits a full simulation of the dynamic behavior of electric vehicle batteries involving hundreds of discharge and recharge cycles.¹⁵

Results and Discussion

In this section, we benchmark the present micro-macroscopic model against the "exact" solutions developed by De Vidts and White⁷ and De Vidts et al.¹² using the pseudo two-dimensional approach for a Ni-Cd cell and a single MH electrode. Subsequently, we present new results for the discharge and charge of a Ni-MH cell with oxygen evolution and recombination taken into account.

For comparison, we used the same parameters as in Ref. 7 and 12 in the simulations for the discharge of the Ni-Cd cell and the single MH electrode, see Table I. There were, however, a few changes in the parameters used for the full Ni-MH cell, as noted in parentheses in Table I. These include: (i) the maximum theoretical charge per unit of projected electrode area of the MH electrode, $Q_{o,\text{MH}}$; (ii) the initial, maximum, and reference concentrations of atomic hydrogen in MH particles, c_o^{H} , $c_{\text{max}}^{\text{H}}$, and $c_{\text{ref}}^{\text{H}}$; and (iii) the initial and reference concentrations of the electrolyte, c_o^{OH} and $c_{\text{ref}}^{\text{OH}}$. These values are modified to match the theoretically maximum electrode capacity of the MH electrode with that of the nickel electrode. In other words, the capacity ratio of the two electrodes in the simulated Ni-MH cell is equal to unity. The properties of the electrolyte KOH, including D^{OH} , κ , and $c^{\text{OH}}/c^{\text{H}_2\text{O}}$, are expressed as functions of the electrolyte concentration, c^{OH} , as shown in Table II.

Discharge curves to be presented are plotted against the depth of discharge of an electrode or a cell (DOD), which is defined as

$$\text{DOD} = \frac{|I|t}{Q_o} \quad [41]$$

where t is the time elapsed from the beginning of discharge and Q_o is the maximum capacity per unit of projected electrode area of an electrode. Both Ni-Cd and Ni-MH cells are generally designed to be positive-limited to avoid hydrogen evolution on the negative electrode at nearly full charge and overcharge. Thus, Q_o used to define the DOD of a cell should be equal to the capacity of the nickel electrode. The predicted cell potential is defined as

$$\text{Cell potential} = \phi_s(x = L) - \phi_s(x = 0) \quad [42]$$

For a single MH electrode, the electrode potential shown in the following figures is defined as the difference between the potentials at the electrode/current collector boundary and at the electrode/separators interface

$$\text{Electrode potential} = \phi_e(x = L_e) - \phi_s(x = 0) \quad [43]$$

The potential drop in the electrolyte across the electrode is defined as

$$\text{Potential drop in the electrolyte} = \phi_e(x = 0) - \phi_e(x = L_e) \quad [44]$$

Discharge of a Ni-Cd cell.—Figure 2 shows the predicted Ni-Cd cell potential vs. DOD at two different discharge rates in comparison with De Vidts and White's results.⁷ Generally, it is seen that the cell potential decreases gradually over a large range of DOD and then quickly drops to the cutoff voltage near the end of discharge. The end of discharge is caused by an abrupt increase in the proton concentration at the electrode/electrolyte interface and hence the substantial increase in the ohmic resistance inside the nickel active layer. Recall that the nickel electrode behaves like an insulator when the proton concentration reaches the maximum. Compared to the more "exact" solution of De Vidts and White⁷ based on a pseudo two-dimensional numerical approach, the present model yields very similar discharge curves with a discrep-

Table I. Input parameters to numerical simulations.^{7,12}

Nickel electrode	
Specific surface area of nickel substrate, a_{ab}	2000 cm ² /cm ³
Specific electroactive surface area, a_{Ni}	3864 cm ² /cm ³
Exchange current density, $i_{0,ref}$	6.1 × 10 ⁻⁵ A/cm ²
$i_{0,ref}$	1.0 × 10 ⁻¹¹ A/cm ²
Electrode thickness, L_e	0.036 cm
Radius of nickel substrate, r_o	1.5 × 10 ⁻⁴ cm
Radius of nickel active layer, r_s	2.9 × 10 ⁻⁴ cm
Open-circuit potential, $U_{1,ref}$ vs. Hg/HgO	0.427 V
$U_{2,ref}$ vs. Hg/HgO	0.3027 V
Transfer coefficients, α_{ai}, α_{ci}	0.5, 0.5
α_{a2}, α_{c2}	1.5, 0.5
Porosity of nickel substrate, ϵ_b	0.85
Porosity of the electrode, ϵ_{Ni}	0.44
Diffusion coefficient of proton, D^H	4.6 × 10 ⁻¹¹ cm ² /s
Maximum concentration of proton, c_{ref}^H	5.2098 × 10 ⁻² mol/cm ³
Reference concentration of proton, c_{ref}^H	2.6049 × 10 ⁻³ mol/cm ³
Initial concentration of proton, c_i^H	1.0418 × 10 ⁻² mol/cm ³
Maximum charge capacity, $Q_{o,Ni}$	20.6 × 10 ⁻³ Ah/cm ²
Cadmium electrode	
Maximum specific electroactive surface area, $a_{Cd,max}$	4000 cm ² /cm ³
Exchange current density, $i_{03,ref}$	6.1 × 10 ⁻⁵ A/cm ²
$i_{04,ref}$	1.0 × 10 ⁻¹⁴ A/cm ²
Electrode thickness, L_e	0.04 cm
Open circuit potential, $U_{3,ref}$ vs. Hg/HgO	-0.9063 V
$U_{4,ref}$ vs. Hg/HgO	0.3027 V
Transfer coefficients, α_{a3}, α_{c3}	1.0, 1.0
α_{a4}, α_{c4}	1.5, 0.5
Maximum porosity of the electrode, $\epsilon_{Cd,max}$	0.64
Minimum porosity of the electrode, $\epsilon_{Cd,min}$	0.42
Initial porosity of the electrode, $\epsilon_{Cd,o}$	0.64
Molecular weight, $M_{Cd}^{Cd(OH)_2}$	112.4 g/mol
$M_{Cd}^{Cd(OH)_2}$	146.4 g/mol
Density, ρ_{Cd}^{Cd}	8.64 g/cm ³
$\rho_{Cd(OH)_2}^{Cd}$	4.79 g/cm ³
Metal hydride electrode	
Specific electroactive surface area, a_{MH}	2100 cm ² /cm ³
Exchange current density, $i_{03,ref}$	2.84 × 10 ⁻⁴ A/cm ²
Electrode thickness, L_e	0.04 cm
Radius of metal hydride particle, r_s	10 ⁻³ cm
Open circuit potential, $U_{3,ref}$ vs. Hg/HgO	-0.861 V
Transfer coefficients, α_{a3}, α_{c3}	0.23, 0.77
Porosity of the electrode, ϵ_{MH}	0.3
Diffusion coefficient of hydrogen, D^H	5 × 10 ⁻¹¹ cm ² /s
Maximum concentration of hydrogen, c_{max}^H	22.41 × 10 ⁻³ mol/cm ³ (27.48 × 10 ⁻³ mol/cm ³)
Reference concentration of hydrogen, C_{ref}^H	22.41 × 10 ⁻³ mol/cm ³ (27.48 × 10 ⁻³ mol/cm ³)
Initial concentration of hydrogen, C_o^H	22.41 × 10 ⁻³ mol/cm ³ (27.48 × 10 ⁻³ mol/cm ³)
Maximum charge capacity, $Q_{o,MH}$	16.8 × 10 ⁻³ Ah/cm ² (20.6 × 10 ⁻³ Ah/cm ²)
Separator	
Thickness, L_s	0.025 cm
Porosity, ϵ_s	0.68
Electrolyte	
Reference concentration of KOH, C^{OH}	6.0 × 10 ⁻³ mol/cm ³ (7.1 × 10 ⁻³ mol/cm ³)
Initial concentration of KOH, C_o^{OH}	6.0 × 10 ⁻³ mol/cm ³ (7.1 × 10 ⁻³ mol/cm ³)
Oxygen	
Diffusion coefficient, D^{O_2}	10 ⁻³ cm ² /s
Reference concentration in the electrolyte, $C_{ref}^{O_2}$	10 ⁻⁷ mol/cm ³
Initial concentration in the electrolyte, $C_o^{O_2}$	10 ⁻²⁰ mol/cm ³
Cell temperature, T	298.15 K

^a Values in parentheses are used in the simulation of Ni-MH cell.

any of ca. 1% in the discharge time. Note that the only difference between the present micro-macroscopic model and De Vidts and White's pseudo numerical model lies in the mathematical treatment of the microscopic phenomena, i.e., the former uses a diffusion length to describe solid-state diffusion and an electric resistance to account for the microscopic ohmic drop inside the active material,

Table II. Properties of the electrolyte at 298.15 K.^{7,12}

Diffusion coefficient, cm²/s
 $D^{OH} = [1.0 - 4.0804(c^{OH})^{1/2} + 286.2c^{OH} - 3809.7(c^{OH})^{3/2} + 14415.0(c^{OH})^2] \times \exp[-10.467 - 8.1607(c^{OH})^{1/2} + 286.2c^{OH} - 2539.8(c^{OH})^{3/2} + 7207.5(c^{OH})^2]$

Specific conductivity, S/cm
 $\kappa = c^{OH} \exp[5.5657 - 6.1538(c^{OH})^{1/2} - 13.408c^{OH} - 1705.8(c^{OH})^{3/2}]$

Ratio of electrolyte to water concentrations

$$\frac{c^{OH}}{c_{H_2O}^{OH}} = \exp[-6.8818 + 118.75(c^{OH})^{1/2} - 1030.5c^{OH} + 4004.7(c^{OH})^{3/2}]$$

Mean molar activity coefficient of the electrolyte

$$f_{\pm} = \gamma_{\pm} \left(\frac{\rho_{H_2O}}{\rho - M_r^{KOH} c^{OH}} \right)$$

$$\text{with } \ln \gamma_{\pm} = \frac{-1.1813m^{1/2}}{1 + m^{1/2}} + 0.3848m - 0.03205m^{3/2}$$

$$\rho = 1.0002 + 45.726c^{OH} - 601.63(c^{OH})$$

$$m = \left(\frac{1000c^{OH}}{\rho - M_r^{KOH} c^{OH}} \right)$$

Transference number of OH⁻ $t_{-}^{\circ} = 0.78$

whereas the latter approach uses exact differential equations. The good agreement shown in Fig. 2 thus suggests that the analytical expressions for the species diffusion length and the electrical resistance developed in Part I adequately describe the microscopic solid-state diffusion and ohmic-drop phenomena, at least under simple galvanostatic conditions. Detailed discharge and charge characteristics of Ni-Cd cells have been explored in Ref. 7 and are not repeated here.

Discharge of a MH electrode.—Figure 3 shows discharge curves of a single MH electrode at two different current densities. As expected, the electrode potential is seen to decrease with the DOD, which is partly due to the decrease in the hydrogen concentration in MH particles. The electrode potential drops more quickly at a higher discharge current density because of the quicker consumption of hydrogen at the particle surface. The sharp drops in the electrode potential near the end of discharge at both discharge rates are therefore attributed to the depletion of hydrogen at the MH particle surface. Once again, it can be seen that the present predictions are in excellent agreement with the results of De Vidts et al.¹² for both discharge rates.

Figure 4 shows the potential drop in the electrolyte across the MH electrode as a function of DOD. It is seen that this ohmic loss in the electrolyte is quite small (only

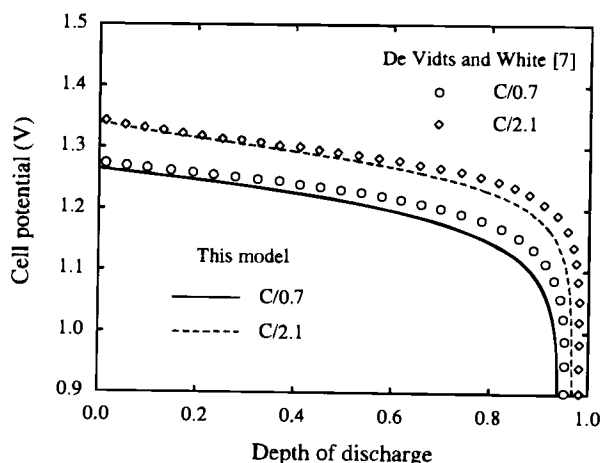


Fig. 2. Predicted Ni-Cd cell potential vs. DOD at different discharge rates.

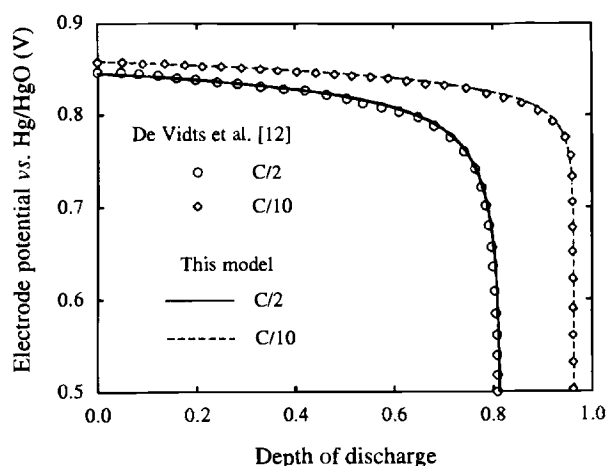


Fig. 3. MH electrode potential vs. DOD at different discharge rates.

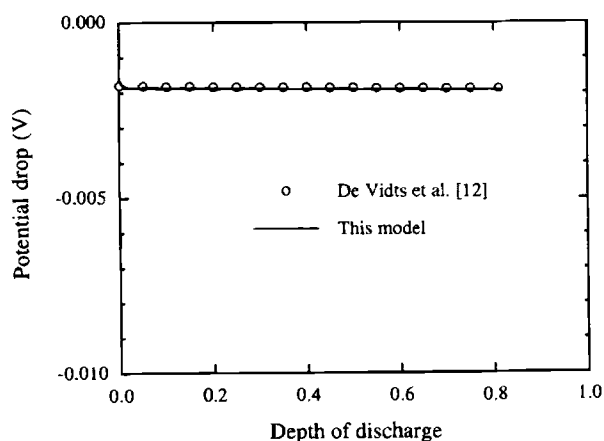


Fig. 4. Potential drop in the electrolyte across the MH electrode as a function of DOD at the C/2 rate.

about 2 mV) due to the combination of small electrode thickness and large ionic conductivity of the KOH solution. A good agreement between the present prediction and the previous result is again seen in Fig. 4. Figure 5 further compares predicted distributions of the hydrogen concentration at the MH particle surface across the electrode with previous results.¹² The agreement shown in this figure is indicative that the diffusion length used in the present model has indeed adequately captured the diffu-

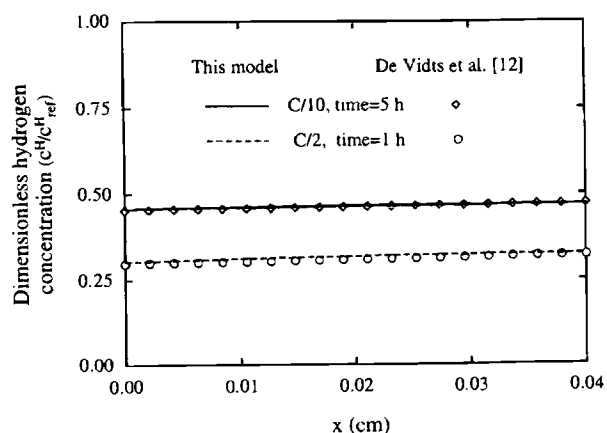


Fig. 5. Representative hydrogen concentration distributions at the MH/KOH interface across the MH electrode in comparison with the results of De Vidts et al.¹²

sion process of hydrogen from the interior of MH particles to the surface during discharge.

Discharge of a Ni-MH cell.—To model discharge and charge characteristics of Ni-MH cells for the first time, computer simulations were performed for a Ni-MH cell with equal charge capacities of the two electrodes. A complete set of model parameters is listed in Table I. Figure 6 shows the discharge cell potential of the Ni-MH cell at three different rates. The discharge curves are, in general, similar in shape to those of the Ni-Cd cell. As explained earlier, the performance of the Ni-Cd cell is limited by proton diffusion in the nickel active material, while the discharge of the MH electrode is controlled by hydrogen diffusion in MH particles. It is therefore expected that the cell performance of a Ni-MH cell may be controlled by either proton diffusion in the nickel active materials or hydrogen diffusion in MH particles. Which mechanism is a more limiting factor would depend on the cell design, particularly on particle sizes and diffusion coefficients of the active material in both nickel and MH electrodes, as well as the ratio of charge capacities of the nickel to MH electrodes.

To explain the cause for the end of discharge of the simulated cell, Fig. 7 shows time-dependent profiles of the volume-averaged concentration of hydrogen in the MH electrode and protons in the nickel electrode during discharge at the rate C/2.1. In general, it can be observed that the proton concentration increases with time while the hydrogen concentration decreases with time during discharge. The trends reverse when charging. The end of dis-

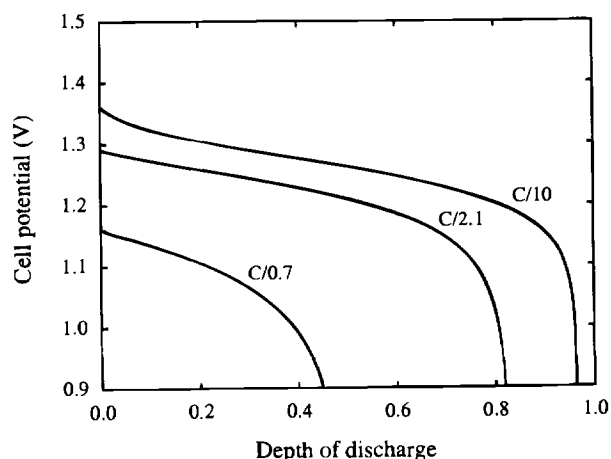


Fig. 6. Predicted Ni-MH cell voltage vs. DOD at different discharge rates.

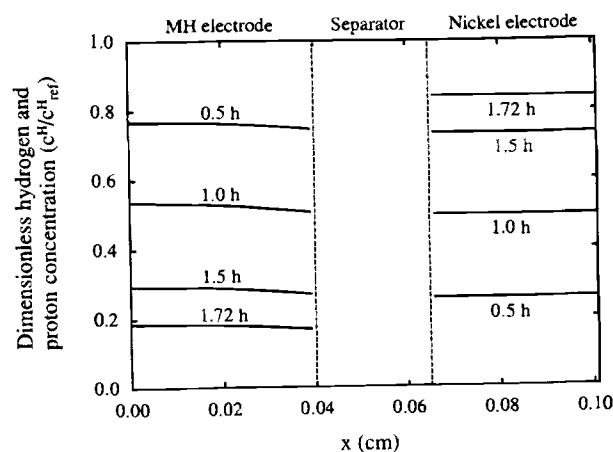


Fig. 7. Profiles of the volume-averaged concentration of hydrogen in MH electrode and protons in the nickel electrode at various discharge times with the C/2.1 rate.

charge in this case is marked by $t = 1.72$ h, at which time there is still a considerable amount of hydrogen available in MH particles and the proton concentration in the nickel active materials has also not yet reached the maximum value, leading to a drastic increase in the overpotential (Fig. 7). However, the profiles of the surface concentration at the same discharge times shown in Fig. 8 illustrate that the surface hydrogen concentration in the MH electrode decreases to virtually zero, whereas the surface proton concentration is still below the maximum value at $t = 1.72$ h. This clearly shows that the present Ni-MH cell is MH electrode-limited. More specifically, solid-state diffusion of atomic hydrogen in MH particles represents the cell-limiting mechanism. In practice, Ni-MH cells are preferred to be positive-limited, and thus the capacity of the MH electrode should be designed to be larger than that of the nickel electrode.

Figure 9 plots the predicted electrolyte concentration distributions in the Ni-MH cell at the end of discharge at C/2.1 and C/0.7 rates. The initial concentration is equal to 7.1 M. Whereas the average electrolyte concentration is seen to remain at the initial value, the electrolyte concentration is slightly below the initial value due to the consumption of OH^- in the MH electrode and above the initial value due to the generation of OH^- in the nickel electrode. However, across the cell there is neither accumulation nor consumption of OH^- during discharge and charge of Ni-MH cells. This behavior is different from that of Ni-Cd cells in which the average concentration of the electrolyte

increases with time at discharge due to the consumption of water (the solvent) and decreases at charge because of the production of water. The nearly uniform electrolyte concentration distributions shown in Fig. 9 indicate that the mass transfer in the electrolyte is not a factor limiting the performance of the Ni-MH cell.

Charge of a Ni-MH cell.—The present model is also capable of simulating cell charge and overcharge in the presence of gas generation and recombination. These overcharge mechanisms are important to the operation of cells, particularly for cells in series. Figure 10 displays the simulation results for the Ni-MH cell overcharged at two different rates, taking into account the oxygen evolution at the nickel electrode and oxygen recombination at the MH electrode. It can be seen that a potential plateau characteristic of gas evolution and recombination is successfully captured by the model. A detailed study of gas evolution and recombination in Ni-MH cells, coupled with careful experimentation, is deferred to a future publication.

Conclusions and Future Work

The micro-macroscopic coupled model developed in Part I has been successfully applied to predict discharge and charge behaviors of Ni-Cd and Ni-MH cells. The model systematically integrates microscopic solid-state physics into macroscopic calculations of species and charge transfer. The model predictions have been validated against the previous results available in the literature for a Ni-Cd cell and a single MH electrode with good agreement. As compared to the pseudo two-dimensional numerical model, the present model offers a more efficient

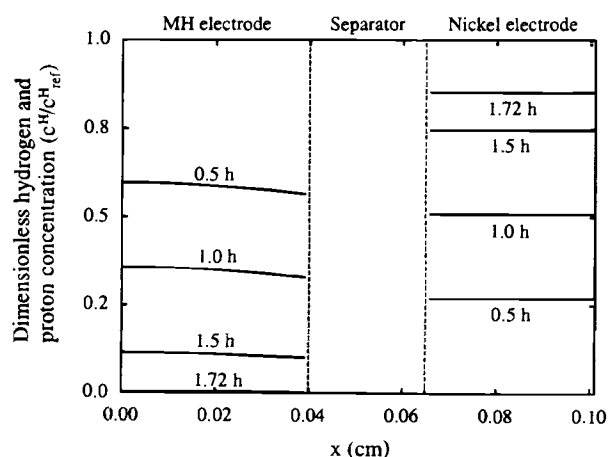


Fig. 8. Profiles of surface concentration of hydrogen in the MH electrode and protons in the nickel electrode at various discharge times with C/2.1 rate.

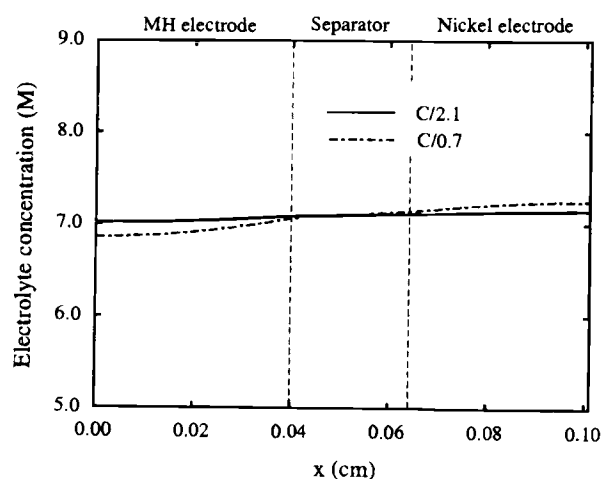
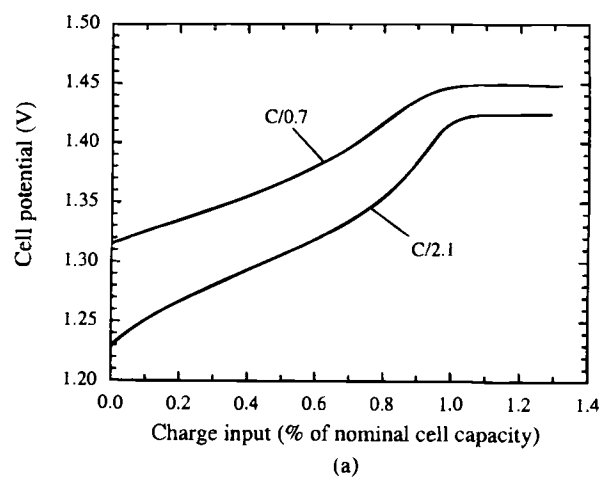
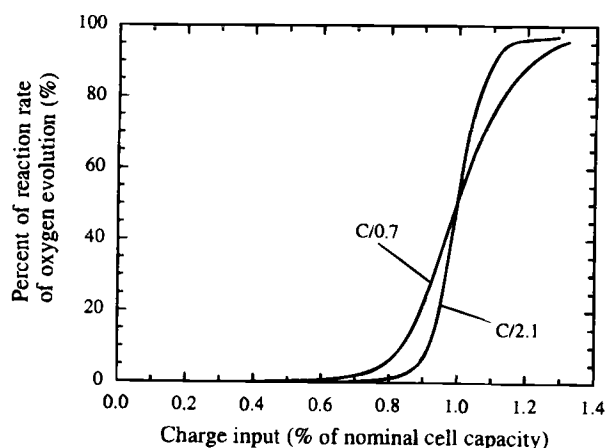


Fig. 9. Predicted electrolyte concentration distributions in the Ni-MH cell at the end of discharge for C/2.1 and C/0.7 rates.



(a)



(b)

Fig. 10. Simulation results for the Ni-MH cell during charge and overcharge at different charging rates: (a) cell potential and (b) percent of the reaction rate of oxygen evolution.

approach to the modeling of intercalative batteries and can be more easily applied to simulate complex cycles of discharge, rest, and recharge as involved in the electric vehicle application.

Computer simulations for discharge and recharge of a Ni-MH cell have been performed. The new results have shown somewhat different behaviors of Ni-MH cells from that of Ni-Cd cells. In particular, it was revealed that both hydrogen diffusion in MH particles and proton diffusion across the nickel active material can be dominant mechanisms limiting cell performance, depending on the ratio of charge capacities of the two electrodes. Such basic knowledge of Ni-MH cells would help in the design and optimization of Ni-MH batteries for various consumer applications and electric vehicles.

Efforts are currently underway to further validate the present Ni-MH model against experimental data. In addition, potential applications of the present Ni-MH model are being pursued to develop an integrated simulation and testing scheme to evaluate electric vehicle batteries and study pulse charging of Ni-MH batteries for rapid rechargeability.

In closing, the present micro-macroscopic modeling framework can also be extended: (i) to study gas evolution and recombination in recombinant batteries more rigorously by permitting the presence of a separate gas phase;¹⁷⁻¹⁸ (ii) to incorporate thermal effects along with the solid-state diffusion in high power applications; and (iii) to develop new models for other battery systems such as lithium-ion batteries.

Acknowledgment

This work is supported in part by the Defense Advanced Research Projects Agency (DARPA), Tactical Technology Office, Electric Vehicle Technology Program, under cooperative agreement No. MDA972-95-2-0009.

Manuscript submitted December 3, 1997; revised manuscript received June 19, 1998.

University of Hawaii at Manoa assisted in meeting the publication costs of this article.

LIST OF SYMBOLS

a	specific interfacial area, cm^2/cm^3
c^i	volume-averaged concentration of species i over a phase, mol/cm^3
\bar{c}_{se}^i	area-averaged concentration of species i over the solid/electrolyte interface, mol/cm^3
D^i	diffusion coefficient of species i in a phase, cm^2/s
F	Faraday's constant, 96,487 C/mol
f_{\pm}	mean molar activity coefficient of the electrolyte
I	applied current density, A/cm^2
i_{nj}	area-averaged transfer current density of reaction j , A/cm^2
$i_{0j,\text{ref}}$	exchange current density of reaction j at reference conditions, A/cm^2
j^i	reaction current density due to production or consumption of species i , A/cm^3
L	cell width, cm
L_e	electrode thickness, cm
l_{se}	diffusion length of species from solid/electrolyte interface into solid phase, cm
M_i^0	molecular weight of species i , g/mol
Q_o	maximum charge per unit of projected area of the electrode, C/cm^2
R	universal gas constant, 8.3143 J/mol K
R_{sb}	electrical resistance from solid/substrate interface to the bulk of solid, $\Omega \text{ cm}^2$
R_{se}	electrical resistance from solid/electrolyte interface to the bulk of solid, $\Omega \text{ cm}^2$
r	radial coordinate, cm
r_c	radius of cylinder substrate, cm
r_s	radius of cylinder or sphere of electrode active material, cm
S	source term in Eq. 38
S_c	constant part of source term
S_p	linear part of source term
T	absolute temperature of the cell system, K
t	time, s
t_{∞}^o	transference number of OH^- with respect to the

$U_{j,\text{ref}}$	open-circuit potential for reaction j at reference conditions measured with respect to a Hg/HgO reference electrode, V
x	x coordinate, cm
Greek	
α_{aj}, α_{cj}	anodic and cathodic transfer coefficients for reaction j
β	morphology correction factor for the conductivity of the cadmium electrode in Eq. 30
Γ	diffusion coefficient pertinent to the general conservable quantity Φ in Eq. 38
ϵ	volume fraction of a phase in the reference elementary volume (REV)
η_j	surface overpotential of electrode reaction j , V
κ	conductivity of an electrolyte, S/cm
κ_D	diffusion conductivity of an electrolyte, A/cm
ρ_i^0	density of species i , g/cm^3
σ	conductivity of the active material in the electrode, S/cm
τ	morphology correction factor for the specific interfacial area of the cadmium electrode in Eq. 33
ϕ	potential in a phase, V
Φ_{se}	average surface potential of solid phase over solid-electrolyte interface, V
Φ	a general conservable quantity in Eq. 38
Subscript	
b	substrate
Cd	cadmium electrode
e	electrolyte
eff	effective
MH	metal hydride active material
max	maximum value
min	minimum value
Ni	nickel active material
ref	with respect to a reference state
s	solid phase
sb	solid/substrate interface
se	solid/electrolyte interface
o	initial value
Superscript	
eff	effective
H	species hydrogen or proton
H_2O	solvent water
OH	species OH^-

REFERENCES

1. C. Y. Wang, W. B. Gu, and B. Y. Liaw, *J. Electrochem. Soc.*, **145**, 3407 (1998).
2. T. F. Fuller and J. Newman, in *Modern Aspects of Electrochemistry*, R. E. White, J. O'M Bockris, and B. E. Conway, Editors, Vol. 27, p. 359, Plenum Press, New York (1995).
3. J. Bouet, F. Richard, and P. Blanchard, in *Nickel Hydroxide Electrodes*, D. A. Corrigan and A. H. Zimmerman, Editors, PV 90-4, p. 260, The Electrochemical Society Proceedings Series, Pennington, NJ (1990).
4. J. W. Weidner and P. Timmerman, *J. Electrochem. Soc.*, **141**, 346 (1994).
5. D. Fan and R. E. White, *J. Electrochem. Soc.*, **138**, 17 (1991).
6. D. Fan and R. E. White, *J. Electrochem. Soc.*, **138**, 2952 (1991).
7. P. De Vidts and R. E. White, *J. Electrochem. Soc.*, **142**, 1509 (1995).
8. B. V. Ratnakumar, P. Timmerman, C. Sanchez, S. D. Stefano, and G. Halpert, *J. Electrochem. Soc.*, **143**, 803 (1996).
9. J. Newman, *Electrochemical Systems*, Prentice Hall, Englewood Cliffs, NJ (1991).
10. M. Viitanen, *J. Electrochem. Soc.*, **140**, 936 (1993).
11. M. Jain and J. W. Weidner, in *Hydrogen and Metal Hydride Batteries*, P. D. Bennett and T. Sakai, Editors, PV 94-1, p. 219, The Electrochemical Society Proceedings Series, Pennington, NJ (1994).
12. P. De Vidts, J. Delgado, and R. E. White, *J. Electrochem. Soc.*, **142**, 4006 (1995).
13. J. K. Heikonen, K. Vuorilehto, and T. Noponen, *J. Electrochem. Soc.*, **143**, 3972 (1996).
14. B. Paxton and J. Newman, *J. Electrochem. Soc.*, **144**, 3818 (1997).
15. W. B. Gu, C. Y. Wang, and B. Y. Liaw, Abstract 100, p. 117, The Electrochemical Society Meeting Abstracts, Vol. 97-1, Montreal, Quebec, Canada, May 4-9, 1997.

16. S. V. Patankar, *Numerical Heat Transfer and Fluid Flow*, Hemisphere, Washington, DC (1980).
17. D. M. Bernardi and M. K. Carpenter, *J. Electrochem.*

- Soc.*, **142**, 2631 (1995).
18. J. Newman and W. Tiedemann, *J. Electrochem. Soc.*, **144**, 3081 (1997).

Mechanistic Aspects of Phenol Electrochemical Degradation by Oxidation on a Ta/PbO₂ Anode

Noureddine Belhadj Tahar, and André Savall*

Laboratoire de Génie Chimique, CNRS UMR 5503, Université Paul Sabatier, 31062 Toulouse Cedex, France

ABSTRACT

The electrochemical oxidation of phenol in an aqueous solution is a complex transformation involving several transfer steps of oxygen atoms and electrons. Transfer of the oxygen atom occurs through the intermediary of hydroxyl radicals adsorbed on the active sites of the anode. Galvanostatic electrolyses of phenol (10.5 to 105 mmol dm⁻³) in aqueous solution at pH 2 on a Ta/PbO₂ anode were followed by high-pressure liquid chromatography and by analysis of the total organic carbon. Hydroquinone, catechol, 1,4-benzoquinone (1,4-BQ), maleic and fumaric acids, and carbon dioxide are the main products. The unidentified products consist mainly of polymers. Study of the influence of temperature shows that the rate consumption of phenol initially at 21 mmol dm⁻³ is mass transport limited. CO₂ is immediately formed following the 1,4-BQ-maleic acid pathway involving 20 faradays and forming 4 mol of CO₂ and/or the 1,4-BQ-intermediary in C2 pathway at 16 faradays with formation of 2 mol of CO₂. The faradaic yield values show that a phenol molecule adsorbed on a catalytic site undergoes a succession of oxidation steps involving, on average, five electrons without desorption of the intermediate products. This number of electrons varies according to the operating conditions (temperature, anodic current density, initial phenol concentration, hydrodynamic conditions, etc.). The mean faradaic yield decreases during electrolysis; it can reach 70% at the beginning of electrolysis of a 21 mmol dm⁻³ phenol solution for an anodic current density of 100 mA cm⁻². The phenol conversion into insoluble polymers increases as a function of its initial concentration and the anodic current density but it does not exceed 10%.

Introduction

Generally, electrochemical oxidation of an organic compound in aqueous solution does not result from a direct transfer of electrons between the electrode surface and the reagent. In fact, it is a transfer reaction of one or more oxygen atoms. In the case of phenol, oxidation occurs in accordance with a complex mechanism involving both transfer of oxygen atoms and direct transfer of electrons.¹

It is often assumed that the first step of oxygen transfer is the water molecule discharge at one electron leading to the formation of a hydroxyl radical (OH•) adsorbed on an active site of the anode surface.²⁻⁸ The second step is an electrophilic attack of the hydroxyl radical on the organic compound transported from the bulk of the solution to the electrode interface. Any organic compound can thus theoretically be oxidized on classical anode materials such as Au, Pt, C, etc., if the electrode potential value is sufficient to form the hydroxyl radicals. However, on these anode materials, the oxygen transfer reactions are slow and are characterized by low faradaic yields; in fact, a loss of current occurs with the formation of molecular oxygen.⁹⁻¹⁴ Thus, to oxidize an organic compound in a water solution, an anode material with a high oxygen overpotential should be used. Among the materials which meet this criteria are tin(IV) dioxide,^{13,15} synthetic diamond,¹⁶ and lead(IV) dioxide.¹⁷ Lead dioxide used for this work has a good electrical conductivity and can be easily prepared by electrochemical oxidation of lead nitrate solution.

Electrochemical oxidation of phenol in an aqueous solution has been the subject of many studies.^{2,9,12,13,15,18-20} In the first step, the phenol oxidizes successively to hydroquinone (HQ) then into 1,4-benzoquinone (1,4-BQ); parallel with the hydroquinone, catechol (Cat) also forms in small quantities. Then, oxidation of 1,4-BQ leads, after opening of the aromatic ring, to the formation of aliphatic carboxylic acids such as maleic acid (M. A.) and fumaric acid (F. A.).^{9,13} The final products of the phenol degradation are carbon dioxide and water. The complete phenol degradation through to the CO₂ and water stage requires, overall, an exchange of 28 electrons by direct and indirect

transfer. The mechanism involved is highly complex, due to the high reactivity of the hydroxyl radicals vs. the adsorbed organic substances.

In this work, we have studied the kinetics of the electrochemical oxidation of phenol in acidic aqueous solution on Ta/PbO₂ electrodes. The electrolyses were performed by following the concentrations of the main intermediate products formed as well as the value of total organic carbon (TOC). The influence of temperature, the initial concentration of phenol, and the anodic current density were studied to further our understanding of the mechanism of electrochemical degradation of phenol.

Experimental

Preparation of the Ta/PbO₂ electrode.—The deposit of lead dioxide is made by electrochemical oxidation of an aqueous solution of lead nitrate on a rectangular plate of massive tantalum (70 × 10 × 1 mm). Tantalum has been chosen for reasons of chemical and electrochemical stability. Tantalum is highly stable in acidic medium; its corrosion resistance is due to the formation of a protective oxide layer.²¹ From the potential-pH equilibrium data, tantalum undergoes passivation on contact with an aqueous solution by formation of a nonconducting oxide layer Ta₂O₅.²² Nevertheless, the lead dioxide can be deposited on the tantalum substrate if the operation is carried out slowly.

Surface treatments.—With the aim of, on the one hand, obtaining a rough surface which can be reproduced and, on the other, increasing the adhesion of the PbO₂ deposit on the tantalum substrate, the latter was subjected to mechanical abrasion by sand blasting with grains of 0.3 mm av diam at a pressure of 5 bar (Brasfanta 037/320 Bremor, Switzerland). The tantalum substrate was then cleaned using ultrasound for 10 min in order to remove any sand particles lodged on its surface. The average loss in mass per unit of surface area due to the sand blasting is 0.55 ± 0.12 mg cm⁻². The tantalum surface is then chemically stripped for 30 s in 40% hydrofluoric acid at room temperature. This chemical treatment dissolves the layer of tantalum oxide which is formed spontaneously on contact with oxygen in the air. The loss in mass per unit of surface area due to this chemical stripping is 0.18 ± 0.06 mg cm⁻².

* Electrochemical Society Active Member.